Hemodynamic Computation Using Multiphase Flow Dynamics in a Right Coronary Artery

JONGHWUN JUNG, AHMED HASSANEIN, and ROBERT W. LYCZKOWSKI

Argonne National Laboratory, 9700 S. Cass Avenue, Argonne, IL

Abstract—Hemodynamic data on the roles of physiologically critical blood particulates are needed to better understand cardiovascular diseases. The blood flow patterns and particulate buildup were numerically simulated using the multiphase non-Newtonian theory of dense suspension hemodynamics in a realistic right coronary artery (RCA) having various cross sections. The local hemodynamic factors, such as wall shear stress (WSS), red blood cell (RBC) buildup, viscosity, and velocity, varied with the spatially nonuniform vessel structures and temporal cardiac cycles. The model generally predicted higher RBC buildup on the inside radius of curvature. A low WSS region was found in the high RBC buildup region, in particular, on the area of maximum curvature of a realistic human RCA. The complex recirculation patterns, the oscillatory flow with flow reversal, and vessel geometry resulted in RBC buildup due to the prolonged particulate residence time, specifically, at the end of the diastole cycle. The increase of the initial plasma viscosity caused the lower WSS. These predictions have significant implications for understanding the local hemodynamic phenomena that may contribute to the earliest stage of atherosclerosis, as clinically observed on the inside curvatures and torsion of coronary arteries.

Keywords—Multiphase, Particulate buildup, Computational fluid dynamics, Wall shear stress, Non-Newtonian, Secondary flow, Cardiovascular disease.

INTRODUCTION

Atherosclerosis, the most common type of cardiovascular disease,[1] is a geometrically focused disease preferentially located in the inner curvatures of arteries, near side branches, and in the outer wall of bifurcations with complex flow patterns.[3,9,24,37,69] Several studies have shown a strong correlation between hemodynamics and endothelial cell functions in the progression of atherosclerosis lesions.[41,53,58] Possible mechanisms for this correlation depend on the local flow phenomena, the rheological properties of blood, the artery geometry, and the physiological state of the endothelium.[59] Under low wall shear stress (WSS), endothelial cell modulates gene expressions, resulting in random cell structures, a decrease of nitric ox-

ide (NO) production, an increase of monocyte adhesion and migration, and an increase of permeability to macromolecules.[7,11,12,28,53,63,64] Understanding the local hemodynamic parameters in the blood flow of the human artery is critical in the diagnosis and treatment[30,53,61] of patients with cardiovascular disease.

In recent years, single-phase computational fluid dynamics (CFD) techniques, combined with noninvasive medical imaging, have been used increasingly by researchers seeking to better understand hemodynamic factors.[4,12,25,31,44,48,51,56,67,68] Various investigators have reported the coexistence of regions of low WSS and high tensile stress[57,68] and an inverse relationship between WSS and wall thickness.[6,36,37] The increase in wall thickness was initially associated with plaque accumulation on the vessel wall. The lumen area remained unchanged with stenosis less than 40%.[26] After stenoses rose above 40%, however, Wentzel *et al.*[65] observed that the deposition of atherosclerotic plaque and vessel remodeling had no consistent correlation with low WSS. They suggested a growing importance of nonshear-stress-related plaque progression with lumen narrowing. Wall thickness was positively correlated with the curvature and torsion in the human coronary artery and seemed to be influenced by multiple aspects of the dynamic geometry.[69] Zeng *et al.*[67] concluded that WSS is driven by a complex combined effect of local and upstream geometry. Steinman and his colleagues[50,52] indicated that clinical decisions based on computational analyses must employ the actual vessel geometry for an individual's cardiovascular disease, not the idealized vessel geometry, which can only be applied in a general sense to the human circulation.

Additional hemodynamic factors to consider would be the cell interaction effect and the spatial distribution of particulate cells in blood flow for the normal case of about 40% (by volume) red blood cells (RBCs).[43] The motions of RBCs in concentrated suspensions were studied by tracking the particles in flow-through tubes.[27] Non-Newtonian shear thinning with plug flow in the core of the tubes was observed. The RBC viscosity was governed by the deformation of particles. Based on particle interactions in concentrated suspensions, Phillips *et al.*[46]

Address correspondence to Jonghwun Jung, Argonne National Laboratory, Energy Technology Division, Building 308,9700 South Cass Avenue, Argonne, IL 60439. Electronic mail: jungjh@anl.gov

derived a constitutive equation that consists of a stress tensor depending on the particle volume fraction and a diffusion equation accounting for shear-induced particle migration. Based on *in vitro* experimental results, Munn *et al.* described the important role of RBCs in leukocyte rolling, namely, that the RBCs greatly enhance leukocyte adhesion to activated endothelium.[43]

To better understand hemodynamics, several recent studies[34,40,55] have applied multiphase theory to blood flow modeling. In the particle trajectory model for describing the motion of dilute spherical blood cells,[40] the dominant forces proved to be the drag and pressure gradient terms; other contributions were relatively negligible. A model based on near-wall residence time for particulate-wall interactions indicated the probability of blood particulate deposition in femoral bypass graft anastomosis. Sun *et al.*[55] analyzed the interactions between RBCs and leukocytes in a capillary tube using a lattice Boltzmann approach. Our recent work[34] showed that RBC buildup in an idealized coronary artery with the same tube diameter is on the inside radius of curvature.

In this work, the application of multiphase CFD to test the hypotheses of local hemodynamics was undertaken for a realistic human right coronary artery (RCA) using the multiphase non-Newtonian theory of concentrated suspension flows.[34] The model described the motion of the fluid and the particulates using the concept of local mean variables, where the cell interactions and the drag force become important. Of specific interest is particulate deposition and WSS at the curvature of tortuous reduction in area as a function of a cardiac cycle for the geometry effect, like stenosis in a vessel.

METHODS

RCA Geometry

The geometry for a 3-D model of a realistic human RCA was constructed from the views of coronarography (http://flowlab.fluent.com/exercise/coronary.htm), as described in detail by Berthier *et al.*[4] (Fig. 1). By a technique similar to clinical biplane angiography, 30 consecutive cross sections were used to generate a realistic 3-D RCA. The vessel had different cross sections along with variable shapes in the axial direction. From the views of coronarography,[4] two side branches having small diameters [point (5) of Fig. 1] and a main side branch [point (6) of Fig. 1] were observed. In the simulation, we used a long segment of RCA without any side branches. The inlet area was 15 mm^2, and the outlet area was 2.2 mm^2. The total length of the realistic RCA was 0.13 m. A straight entry tube of 20-mm length was attached to the realistic RCA to remove inlet effects on the computed flow field and to ensure a fully developed velocity profile in the blood entering region. A mesh was generated using GAMBIT software (from Flu-

ent Inc.) and a Cooper volume-meshing scheme. A mesh refinement having a total thickness of 0.182×10^{-3} m was used in the vicinity of the wall to better resolve the shear gradient. The total number of nodes used for the generated mesh was 40,734. The total number of elements for the mesh was 36,418 with 278 cross sections of 131 faces per cross section. We adapted this mesh to our multiphase 3-D simulations using GAMBIT software.

Multiphase Governing Equations

A multiphase, non-Newtonian, 3-D CFD model was developed at Argonne National Laboratory for describing the hemodynamics in vascular vessels. It uses the principles of mass, momentum, and energy conservation for each phase. This approach, based on the generalization of the well-known Navier–Stokes equations, is similar to that of Anderson and Jackson[2] and Gidaspow.[22] The principal difference compared with a single-phase model is the appearance of the volume fraction for each phase, as well as mechanisms for the exchange of momentum, heat, and mass between the phases. To solve the conservation equations for hemodynamics, appropriate rheological properties of each phase have to be specified. A modification of the Carreau–Yasuda viscosity model was used to describe the non-Newtonian shear-thinning rheological behavior of blood flow. Gidaspow gives a detailed multiphase flow description in his book.[22]

In the two-phase non-Newtonian hemodynamic model, the continuous phase is plasma, which contains water and various nutrients, minerals, and proteins.[39] The predominant dispersed (particulate) phase suspended in the plasma is RBCs, which have a hematocrit or volume fraction range of roughly 30–55% *in vivo*. Leukocytes or white blood cells and platelets constitute an aggregate volume fraction less than one percent. In this paper only RBCs are modeled since they control the blood rheology.

A general mass balance for each phase (k = plasma, RBCs) is given by

$$\frac{\partial(\rho_k \varepsilon_k)}{\partial t} + \nabla \cdot (\rho_k \varepsilon_k \vec{v}_k) = 0 \qquad (1)$$

where ρ is density, ϵ is volume fraction, t is time, and v is velocity. In addition, the volume fraction of each phase must sum to one as

$$\sum_{k=1}^{np} \varepsilon_k = 1.0 \qquad (2)$$

where np is total number of phases. The volume fraction occupied by one phase cannot be occupied by other phases.

The momentum equation for each phase is given by

$$\frac{\partial(\rho_k \varepsilon_k \vec{v}_k)}{\partial t} + \nabla \cdot (\rho_k \varepsilon_k \vec{v}_k \vec{v}_k) = -\varepsilon_k \nabla p + \nabla \cdot \overline{\overline{\tau}}_k + \varepsilon_k \rho_k \vec{g}$$
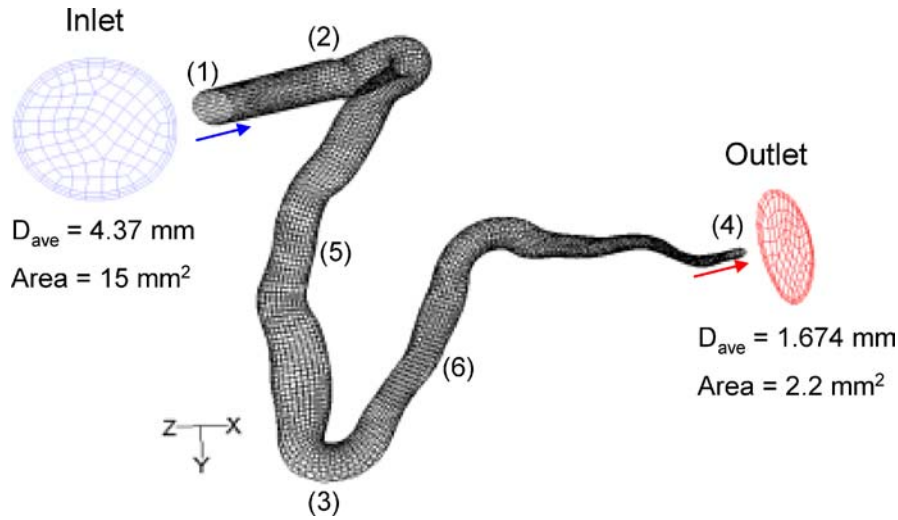$$+ \sum_{l \neq k} \beta_{kl} (\vec{v}_l - \vec{v}_k) + \vec{F}_k \qquad (3)$$

FIGURE 1. 3-D computational mesh for a realistic coronary artery generated using Cooper mesh generation algorithm and GAMBIT software.[4,19] The geometry was reconstructed from the views of coronarography. Point (1): inlet; point (2): the end of a straight entry tube; point (3): maximum curvature; point (4): outlet; and points (5) and (6): the positions of side branches in a real artery.

where p is the pressure, τ is the stress tensor, g is the gravity force, and F is the external forces such as virtual mass, rotational and shear lift, electricity, and magnetism. In the drag force k and l represent plasma or RBCs, and β_{kl} represents the interphase momentum exchange coefficients.

Solving Eqs. (1)–(3) requires several constitutive relations, discussed next.

Constitutive Relations

Mixture Density

The blood mixture density, ρ_{mix}, is given by the sum of the volume-fraction-weighted densities for the plasma and RBCs, neglecting the minor blood-borne constituents:

$$\rho_{\mathrm{mix}} = \varepsilon_{\mathrm{plasma}}\rho_{\mathrm{plasma}} + \varepsilon_{\mathrm{rbc}}\rho_{\mathrm{rbc}} \tag{4}$$

We used a mixture density[65] of 1045 kg/m^3 with an inlet hematocrit of 45% at rest,[16] in which the plasma density was 1003 kg/m^3 and the RBC density[8] was 1096 kg/m^3.

Blood Rheology Model

The rheological model for blood viscosity is a key factor in the simulation of hemodynamic flows. The non-Newtonian shear-thinning model is able to describe the flow in a neutrally buoyant dense suspension at high volume fraction of particles.[14] The Carreau–Yasuda viscosity model was used to simulate single-phase hemodynamics in a carotid artery bifurcation,[25] in which the flattened velocity profiles were as expected for a shear thinning fluid. In our simulation, the dimensionless relative mixture viscosity, η, depends on the shear rate as well as the hematocrit, H, in a way similar to that found by Ding $et\ al.$[14] (Fig. 2).

The dimensionless relative mixture viscosity can be computed from the experimental rheological data for human blood[8,66]:

$$\eta = \frac{\varepsilon_{\mathrm{RBC}}\mu_{\mathrm{RBC}} + \varepsilon_{\mathrm{plasma}}\mu_{\mathrm{plasma}}}{\mu_{\mathrm{plasma}}} = m\left[1 + (\lambda\dot{\gamma})^2\right]^{(n-1)/2} \tag{5}$$

where m, λ, and n are parameters defined below, and $\dot{\gamma} = (\nabla\vec{v} + (\nabla\vec{v})^T)$ is shear rate $(1/s)$. The dimensionless shear rate is given by $1 + (\lambda\dot{\gamma})^2$. In our empirical correlation to the experimental data for the hematocrit range between 30 and 75%, the time constant, λ, is taken to be
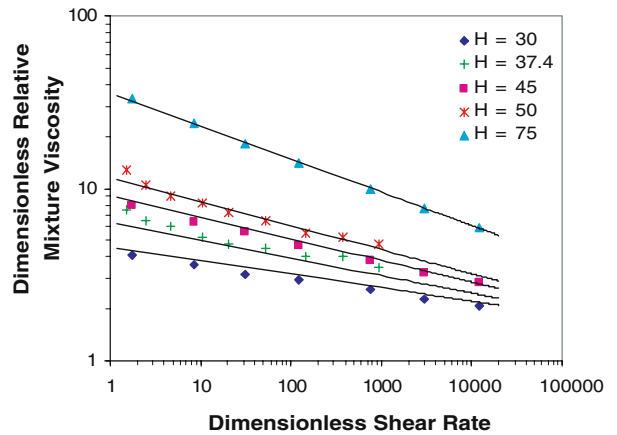

FIGURE 2. Dimensionless relative blood viscosity, η, as function of dimensionless shear rate, $1 + (\lambda\dot{\gamma})^2$ and hematocrit, obtained from experimental data for blood.[8,66] The points represent the experimental data at the different hematocrits and shear rates. The solid lines represent the empirical correlation at the constant hematocrit computed from Eq. (5).

0.110 s, the same as used by Gijsen *et al.*[25] We correlated the two parameters n and m in Eq. (5) as a function of hematocrit, $H = \varepsilon_{\text{RBC}}$, the RBC volume fraction, by the following polynomial approximations:

$$n = 0.8092\varepsilon_{\text{RBC}}^3 - 0.8246\varepsilon_{\text{RBC}}^2 - 0.3503\varepsilon_{\text{RBC}} + 1$$
$$m = 122.28\varepsilon_{\text{RBC}}^3 - 51.213\varepsilon_{\text{RBC}}^2 + 16.305\varepsilon_{\text{RBC}} + 1 \quad (6)$$

As shown in Fig. 2, the dimensionless relative mixture viscosity increases with hematocrit and decreases with increasing dimensionless shear rate, displaying shear-thinning behavior. As the hematocrit goes to zero, Eq. (5) reduces to the Newtonian plasma viscosity. This model is applied to the wider physiological range of hematocrit lower than 75%, where the dimensionless shear rate is between 1.2 and 25,000, corresponding to a shear rate, $\dot{\gamma}$, of between approximately 4 and 1500. Calculations with our empirical mixture viscosity model vary from experimental data,[21,66] near a shear rate of 1000. However, the difference is negligible for low hematocrit.

Plasma Stress Tensor

The stress tensor for the plasma phase is given by the Newtonian form as follows:

$$\overline{\overline{\tau}} = \varepsilon\mu(\nabla\vec{v} + (\nabla\vec{v})^T) + \varepsilon\left(\kappa - \frac{2}{3}\mu\right)\nabla\cdot\vec{v}\overline{\overline{I}} \quad (7)$$

Here, κ and μ are the bulk and shear viscosity for the plasma phase, respectively. ε is volume fraction of plasma, and I is a unit tensor. The plasma bulk viscosity (κ) is assumed to be zero. The plasma viscosity, μ_{plasma}, is treated as a Newtonian fluid having a viscosity of 1 cp.

RBC Stress Tensor

The stress tensor for the RBC phase, the force experienced by the particle as a result of direct contact with other particles,[2,22] is given by the form

$$\overline{\overline{\tau}} = -p\delta + \varepsilon\mu(\nabla\vec{v} + (\nabla\vec{v})^T) + \varepsilon\left(\kappa - \frac{2}{3}\mu\right)\nabla\cdot\vec{v}\overline{\overline{I}} \quad (8)$$

where δ is the Kronecker delta. The RBC pressure p_{RBC} then represents an interparticle pressure as a function of volume fraction of particulate, i.e., ε_{RBC}. This pressure is a result either of the collision of particulates with each other or elastic or inelastic contact between particulates, causing a repulsive force. A compressive force must be applied to bring the particulates closer together. In our RBC-based simulation, the physical constraint that the particulates cannot overlap is assumed to be 90% hematocrit, since blood is fluid even at 98% hematocrit by volume.[21] As a result, the interparticle pressure for a suitable hematocrit range in the simulation is negligibly small. RBC-RBC interactions [Eq. (8)] are represented by the product of effective viscosities and shear rate of the RBCs, where the RBC bulk viscosity (κ) is assumed to be zero. The effective RBC viscosity, μ_{RBC}, is treated as a non-Newtonian shear-thinning fluid calculated from Eq. (5). Hence, it depends on the shear rate and the concentration of RBC, i.e., hematocrit.

External Forces

As a particulate moves through a viscous fluid, a resistance to its motion is caused by the interphase drag. The RBCs behave somewhat like a liquid droplet in blood flow.[21] The interphase momentum exchange coefficients, β, between the plasma and RBCs are determined by the Schiller and Naumann model[19] as

$$\beta = \frac{3}{4}C_d\frac{\rho_{\text{plasma}}\varepsilon_{\text{plasma}}\varepsilon_{\text{RBC}}|\vec{v}_{\text{plasma}} - \vec{v}_{\text{RBC}}|}{d_{\text{RBC}}\phi} \quad (9)$$

where the drag coefficient, C_d, on a single sphere is related to the Reynolds number, Re_p, as

$$C_d = \frac{24}{Re_p}\left[1 + 0.15\,Re_p^{0.687}\right] \quad \text{for} \quad Re < 1000 \quad (10)$$

$$C_d = 0.44 \quad \text{for} \quad Re \geq 1000 \quad (11)$$

$$Re_p = \frac{\rho_{\text{plasma}}\,d_{\text{RBC}}\,|\vec{v}_{\text{plasma}} - \vec{v}_{\text{RBC}}|\,\phi}{\mu_{\text{plasma}}} \quad (12)$$

where d is the diameter of RBCs, and ϕ is the shape factor.

The most important factor for the motion of particulates is the fluid-particulate interaction force as a function of the relative velocity between the plasma and RBCs. The coupling between the momentum equation [Eq. (3)] for the plasma phase and the RBC phase is made explicit by this drag term. As in the case of the mixture equations for components[22], the mixture equations for phases show that the sum of the drag forces in Eq. (3) is zero.

A correction factor called the "shape factor" is added to account for the effect of shape on particulate motion in the drag force. The shapes of particulates (sphere, disk, spheroids, and clusters of spheres) affect the drag force through the drag coefficients and the shape factor. In this simulation, the RBC shape for computing the drag force is assumed to be spherical, i.e., $\phi = 1$. The drag force is an important factor to determine correct flow fields with RBC buildup in the local position. In future studies, its effect on the simulations will be assessed in detail.

Other external forces acting on each phase consist of the virtual mass and shear lift forces. The virtual mass force[19] is given by

$$\vec{F}_{\text{vm}} = 0.5\varepsilon_m\rho_k\left(\frac{d_k\vec{v}_k}{dt} - \frac{d_m\vec{v}_m}{dt}\right)\bigg|_{k \neq m}$$

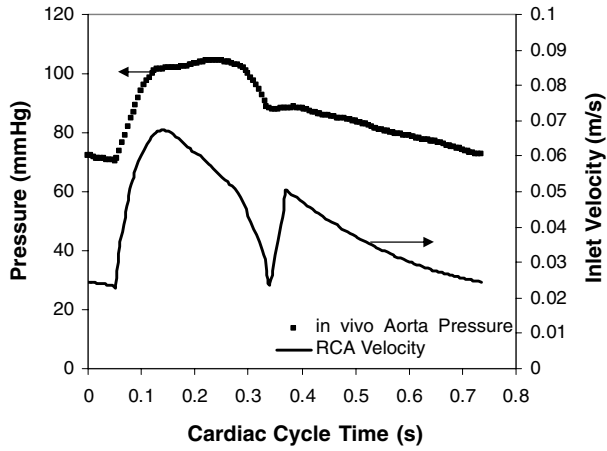$$\left(\vec{F}_{\text{vm},k} = -\vec{F}_{\text{vm},m}\right) \quad (13)$$

FIGURE 3. Inlet velocity waveform generated from RCA blood flow patterns and *in vivo* pressure and flow rate in the ascending aorta.[10,45,47] **Cardiac cycle period: 0.735 s.**

where

$$\frac{d\vec{v}}{dt} = \frac{\partial \vec{v}}{\partial t} + (\vec{v} \cdot \nabla)\vec{v} \qquad (14)$$

The shear lift force is given by

$$\vec{F}_{\text{lift}} = -0.5\varepsilon_m \rho_k (\vec{v}_k - \vec{v}_m) \times (\nabla \times \vec{v}_k)|_{k \neq m}$$
$$(\vec{F}_{\text{lift},k} = -\vec{F}_{\text{lift},m}) \qquad (15)$$

For multiphase flows, the virtual mass effect occurs when a particulate phase accelerates relative to the primary phase. The lift force acts on a particulate mainly due to velocity gradients in the primary-phase flow field. In our coronary artery simulation the estimated virtual mass force and the lift force were negligible.

Numerical Considerations, and Boundary and Initial Conditions

To solve the partial differential equations given above as an initial value problem, the appropriate initial and boundary conditions are critical for the performance of a realistic simulation and comparison with experimental data. To simulate blood flow, we used the commercial code FLUENT 6.1.22,[19] which contains the multiphase 3-D Eulerian–Eulerian model based on the finite-volume unstructured mesh method. The numerical solution method uses a staggered grid arrangement. The scalar variables are located at the cell center, and the vector variables are located at the cell boundaries. The momentum equation is solved with a staggered mesh, while the continuity equation is solved by a donor cell method. For gas-particle flow dominated by convection, the bubble shapes strongly depend on the numerical diffusion introduced by the discretization schemes of the convection terms in the momentum equations.[29,33] Multiphase CFD models have been validated by comparing calculated results with the measured data for spatial and temporal velocities and concentrations obtained from experimental techniques.[22,35] The two-phase CFD model with the non-Newtonian shear-thinning model was initially validated for a neutrally buoyant dense suspension flow.[13,14] The current model in the FLUENT code was successfully applied by reanalyzing NMR slurry measurements[49] for the application of blood flow.[34]

A pulsatile inlet velocity waveform with a cardiac period of 0.735 s was used as an inlet boundary condition for both the RBCs and plasma (Fig. 3). It was generated from blood flow patterns for RCA[45] and *in vivo* pressure and flow rate measured in the ascending aorta.[10,47] The inlet velocity profiles were maintained uniform across the inlet cross section. The boundary condition for zero slip velocity was employed for both RBCs and plasma. The RBCs were considered as spherical particles with a diameter of 8 μm.
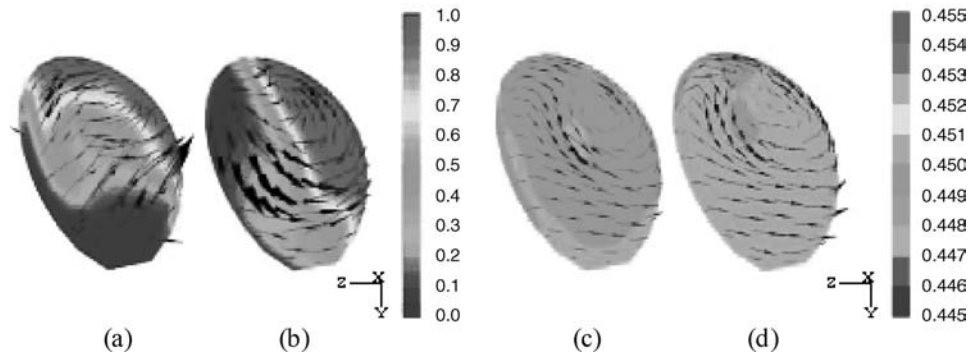

FIGURE 4. Comparison of driving forces [Eq. (3)] determining the motion of red blood cells in the concentrated suspension flow computed by an Eulerian–Eulerian multiphase model. Computational simulations (a) with only the stress tensor term, (b) with the stress tensor and the gravity terms, (c) with the stress tensor and the gravity and the drag terms, and (d) with the gravity and the drag terms. The cross sections were obtained from the maximum curvature [point (3)] indicated in Fig. 1 at 0.16 s. The color indicates the RBC volume fraction, a the vector represents the secondary flow. The direction for gravity is positive *Y*.

The inlet volume fraction of RBCs was maintained steady at 45%. For initial conditions the RBC volume fraction was set to 45%, and both RBC and plasma velocities were set to zero. The FLUENT's outflow boundary condition at the exit was used, where the reference pressure was set to 75 mmHg. The outflow velocity and pressure in the FLUENT code were updated in a manner that was consistent with a fully developed-flow assumption. The maximum residual for convergence of velocity and mass was 10^{-3} using a constant time step of 10^{-4} s on a personal computer having a 3.2-GHz processor running under a Windows system. The average run time for a complete cardiac cycle was $3^3/_4$ h for the multiphase flow and $2^3/_4$ h for the single-phase flow. The non-Newtonian viscosity model for single-phase flow with a constant hematocrit and a density of 1045 kg/m^3 was a function of shear rate alone.

All simulations for the realistic RCA with rigid wall were carried out in the 3-D computational domain. The non-Newtonian shear-thinning viscosity model for RBCs, the transient inlet-mixture velocity waveforms for the cardiac cycle, the lift force model, and the drag force model were programmed into the FLUENT code as individual subroutine files. The computations were run for 21 complete cardiac cycles. Most of the data analysis was performed for the 20th cardiac cycle. Relative RBC buildup was represented as follows:

$$\text{Relative RBC buildup (\%)}$$
$$= \frac{\text{RBC volume fraction} - \text{Initial RBC volume fraction}}{\text{Initial RBC volume fraction}}$$
$$\times 100\% \tag{16}$$

RESULTS

A non-Newtonian shear thinning model was developed for describing the concentrated suspension flow of blood (Fig. 2), as shown in the literature.[5,21,35] The model agreed well with rheological data of blood in the RBC deformation region, except for the very low shear rate obtained with high level of hematocrit.

The RBC motions were estimated using the multiphase hemodynamic model with the developed constitutive relations. Clustering and segregation of particulates occur due to the Bernoulli effect from the change of area, i.e., pressure and velocity fields.[23] The dominant driving forces for the particulate motion are assumed to be the fluid-particulate interactions due to the drag force and the particulate–particulate interactions.[2,22,35] The latter is known as the particulate stress tensor [Eq. (8)] or pressure force. Without the drag force, the simulations predicted the particulate segregation over the whole range of RBC volume fraction between 1.0 and 0 [Figs. 4(a) and 4(b)]. The distributions of the RBC volume fraction approached two limiting cases. The secondary flow was computed to be an order of mag-
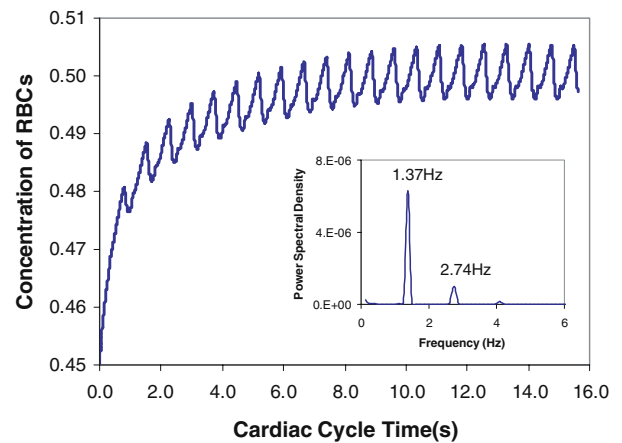

FIGURE 5. Averaged RBC volume fraction as a function of cardiac cycle time at a point of maximum curvature [point (3)] indicated in Fig. 1. Frequency was obtained from between 10th and 20th cardiac cycle.

nitude higher near the lowest limiting case ($\varepsilon_{\text{RBC}} = 0$). The absence of the particulate stress tensor caused a divergence due to the high packing of particulates.

Gravity affected the distribution of RBC volume fraction and the velocity fields. Its effect, however, was reduced by the drag force added to the momentum equations. The model with added drag force [Fig. 4(c)] predicted blood flow with relatively high RBC concentrations in the center. The RBC buildup near the wall was observed in the region of lower absolute pressure in the cross section. Actually, the complete fluid-particulate interactions include the total pressure gradient term in the momentum equation for the particulate phase [Eq. (3)], as described by Anderson and Jackson.[2] Without the particulate stress tensor [Fig. 4(d)], the features of non-Newtonian shear thinning flow disappear. In the simulation, the virtual and lift forces were relatively small compared with the drag force. The difference due to the added forces was two orders of magnitude smaller than when compared with the difference between Fig. 4(c) and Fig. 4(d) indicated by the added stress tensor. The effect of the virtual force was relatively smaller than the lift force at the measured point of the maximum curvature [point (3) of Fig. 1]. The observations for the main driving forces agreed with the results from the multiphase model[22] and the particle trajectory model.[40]

A quasisteady-state condition for the plasma-RBC hemodynamic simulations was established, depending on hemodynamic factors, in which the cardiac events related to valve function were repeated with a period of 0.735 s (Fig. 3). In the single-phase simulations, this condition was established within the fifth cardiac cycle for all hemodynamic factors. In the multiphase simulation, however, it was essentially established by the end of the 14th cardiac cycle (Fig. 5), because a limit cycle behavior of local RBC buildup formed more slowly than other hemodynamic
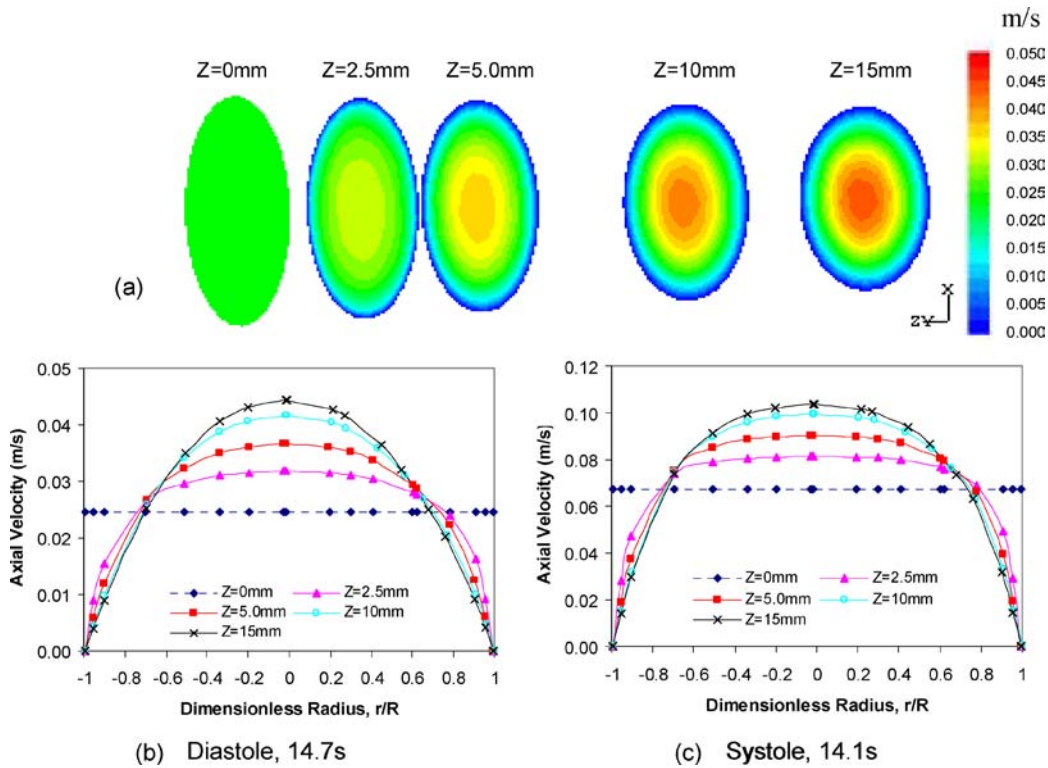
FIGURE 6. Inlet velocity profiles at the entrance region with the additional straight tube of 20 mm between points (1) and (2) of Fig. 1: (a) the axial velocity distributions in the cross sections for the diastole phase at the cardiac cycle time of 14.7 s; (b) the axial velocity profiles at 14.7 s, and (c) 14.1 s. Flow is in the minus direction of the *z*-coordinate. The axial direction is the direction parallel with the vessel tube. The color bar represents the axial velocity.

factors. Local hemodynamic factors oscillated with the main frequency of 1.37 Hz. The second frequency was 2.74 Hz. The frequencies were calculated by fast Fourier transform between the 10th and 20th cardiac cycle.

Local axial velocity varied along the length of the RCA (Figs. 6 and 7) with the inlet velocity waveform generated by the cardiac events of the valve function (Fig. 3). The average flow rate of blood in the inlet was approximately 35 ml/min, corresponding to a mean inlet velocity of 0.042 m/s, as reported in the literature.[4] Inlet velocity profiles were indicated by a partial plug flow in the entrance region of the added straight tube (Fig. 6). The axial peak velocity at the maximum curvature (Fig. 7) reached a value of 0.25 m/s during the systole cycle, and then decreased to zero during the diastole cycle. The velocity distribution in the outlet became almost parabolic with smaller cross-section area.

A feature of non-Newtonian flow was a flat velocity profile in the center region of the added tube (Fig. 6). The entrance length for fully developed laminar flow in the tube is 7.6 mm for a mixture Reynolds number of about 50, based upon classical transport theory.[5] The entrance length of 20 mm for blood flow was sufficient for our simulation. The flow was fully developed within the artery length of 15 mm. In the maximum curvature we are interested, the

axial velocity was predicted to be slightly minus at the end of the diastole cycle [point (4) of Fig. 7(a)]. The curvature-induced secondary flow profiles exhibited a single vortex [Fig. 7(b)]. The magnitude was the same order of magnitude as the axial velocity at the end of the diastole cycle. The recirculation intensity of the secondary flow also varied during the cardiac cycle. The extent of RBC buildup generally increased with the aorta valve closure, before the beginning of the diastole phase in each cardiac cycle, and decreased during the systole phase.

In the long segment of RCA including the inlet and outlet area, we found that the computed local hemodynamic factors such as RBC volume fraction and WSS vary along the length of this artery, which has non-uniform geometry and diameter (Fig. 8). The non-Newtonian multiphase CFD model generally predicted RBC buildup on the inside radius of curvature of a realistic human RCA [Fig. 8(a)]. In particular, the simulation predicted higher RBC buildup with a volume fraction of about 0.55 on the area of maximum curvature just upstream of a tortuous reduction in area. Such a distinguishing mark is due to the segregation of blood-borne particulates in the multiphase CFD model.

The WSS distribution [Fig. 8(b)] showed a similar trend to that observed with the single-phase CFD model. Compared with other RCA areas, the WSS in the inlet area is
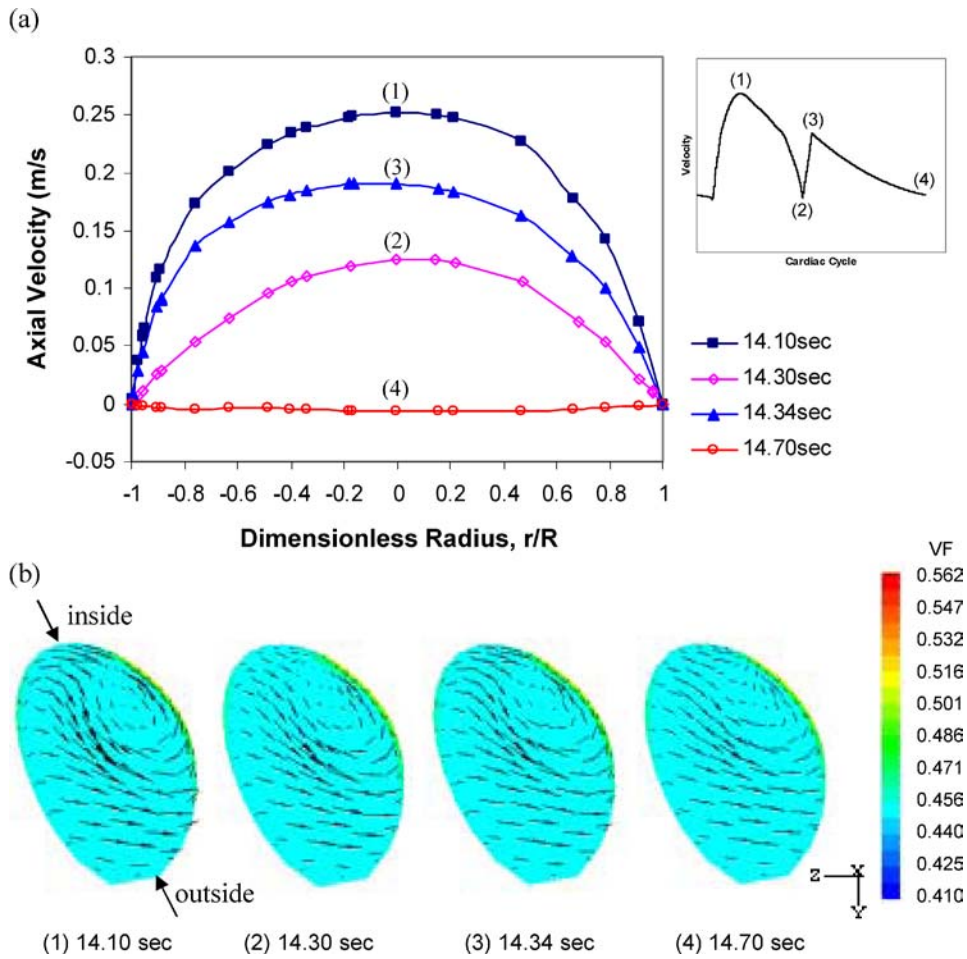
FIGURE 7. Profiles of (a) axial velocity and (b) curvature-induced secondary flow obtained from the cross section (153th cell from the entrance) of point (3) indicated in Fig. 1. The flow direction is from the front to the back. Inside: $r/R = 1$, and outside: $r/R = -1$. Cardiac cycle period: 0.735 s. The axial direction is the direction parallel with vessel tube.
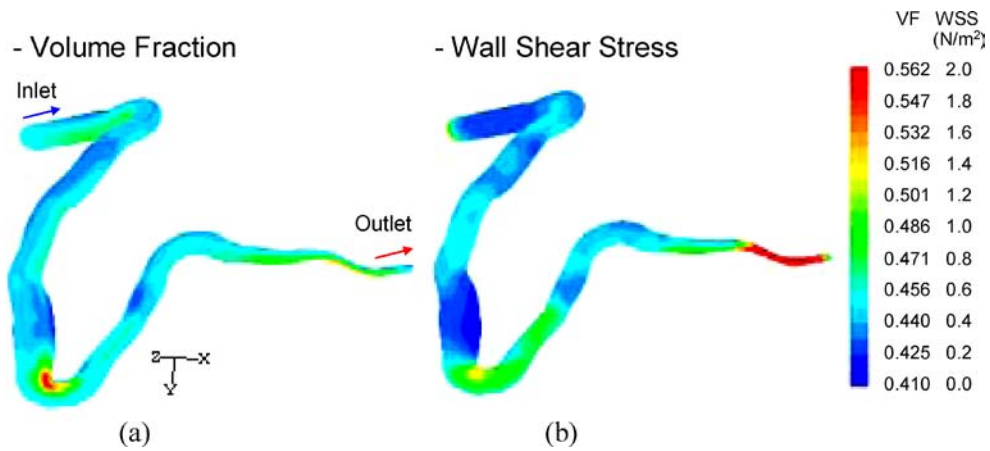

FIGURE 8. Variations of hemodynamic factors in a long segment RCA: (a) volume fraction (VF) and (b) wall shear stress (WSS) of red blood cells (RBC) at the diastole cycle (the cardiac cycle time = 14.7 s, 20th cardiac cycle). The color bar indicates the range of hemodynamic factors.
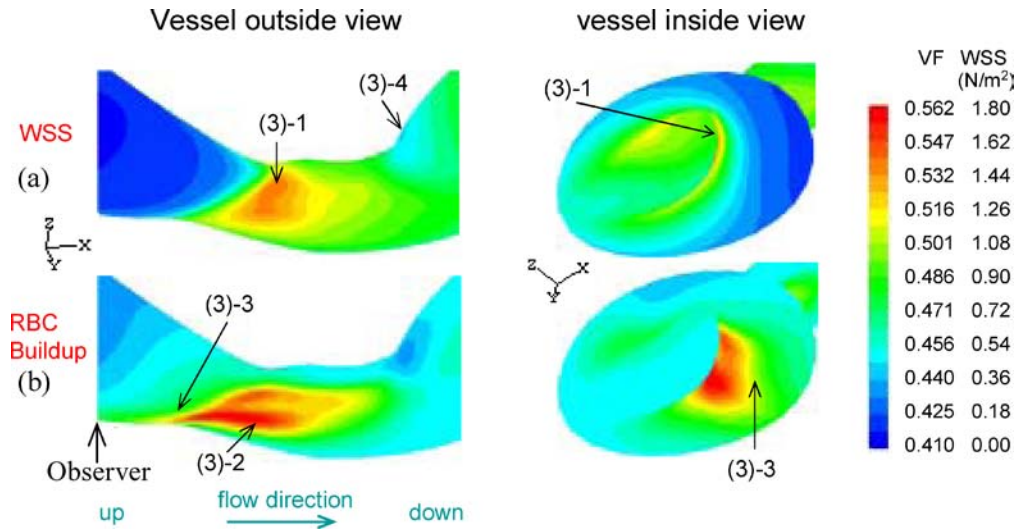
FIGURE 9. Hemodynamic factors near the maximum curvature (point (3) of Fig. 1): (a) wall shear stress and (b) volume fraction of RBC from vessel outside view and vessel inside view at the diastole cycle. (3)-1: the maximum WSS point; (3)-2: the maximum RBC buildup point; (3)-3: the upflow point; and (3)-4: the downflow point with low WSS in the maximum curvature [point (3)] indicated in Fig. 1. (cardiac cycle time = 14.7 s, 20th cardiac cycle).

higher due to the entrance effect having high shear rates near the vessel wall. The WSS in the outlet area was predicted to be highest (maximum 6 N/m^2), because of the smaller cross-section area with a high flow rate. This prediction may be affected by the absence of the main side branch [point (6) in Fig. 1] in the RCA. The computed average local WSS (Fig. 8(b)), except for inlet and out areas, was in agreement with the WSS range being between 0.33 and 1.24 N/m^2, which was measured from the Doppler wire and angiographic technique in the coronary artery.[17] The measured mean WSS was about 0.7 N/m^2 for the flow rate of 35 ml/min used in this study.

Of specific interest is the region of maximum curvature (Fig. 9), where RBC volume fraction generally increased with the high WSS. However, the point of maximum RBC buildup [point (3)-1] did not match the point with highest WSS [point (3)-2]. Compared with RBC buildup just upstream, WSS showed a sharp falling curve followed by a slower decline [near the point (3)-3]. In the downstream area, we found a low RBC volume fraction on the inside radius of the curvature with low WSS [point (3)-4]. From the viewpoint of the vessel inside, near the tortuous reduction area, the WSS was lower than 0.5/N/m^2 with RBC buildup over the volume fraction of 0.5 [point (3)-3]. Low WSS and RBC buildup were related near a tortuous reduction area of the maximum arterial curvature. To better understand this finding, more results were presented by analyzing the temporal variations in the hemodynamic factors at the four points indicated in Fig. 9.

The hemodynamic factors predicted by the single-phase and multiphase non-Newtonian CFD models also varied with the cardiac cycle time (Figs. 10 and 11). The WSS profiles were similar to the inlet velocity waveform (Fig. 3). The viscosity profiles were the opposite: when the aorta valve closed, the viscosity was high. We found that most of the contribution to the hemodynamic forces is due to the RBCs. The WSS from the multiphase model was generally lower than that of the single-phase model. This difference is due to the shear thinning behavior having a lower shear rate in the multiphase flow. The viscosity waveform follows an inverse process of the shear rate waveform. In comparing the maximum WSS point [Fig. 10(a) and 10(c)] and the maximum RBC buildup point [Fig. 10(b) and 10(d)], the viscosities calculated from the multiphase model were higher than those of the single-phase model [Fig. 10(c) and 10(d)]. Low WSS was computed in the highest RBC buildup region [Fig. 10(b)], where the multiphase CFD model showed the small-scale WSS oscillations that were not possible to compute using the single-phase CFD model. The viscosity in this region [Fig. 10(d)] was higher due to the high RBC volume fraction compared with that of Fig. 10(c). This finding shows the dependency of RBC volume fraction in our non-Newtonian viscosity model (Fig. 2). The viscosity in the upflow region was highest for RBC volume fractions over 0.5 [Fig. 11(c)]. Low WSS (less than 1.0 N/m^2) was computed in this region [Fig. 11(a)]. Compared with the upflow region, low WSS also was observed in the downflow region [Fig. 11(b)]. This region showed low viscosity similar to that of the single-phase model and a slightly low, but relatively constant RBC volume fraction [Fig. 11(d)]. We found that low WSS appears near the RBC buildup on the inside radius of the maximum curvature.

Hydrodynamic parameters, averaged for a complete cardiac cycle, also varied with the initial plasma viscosity and
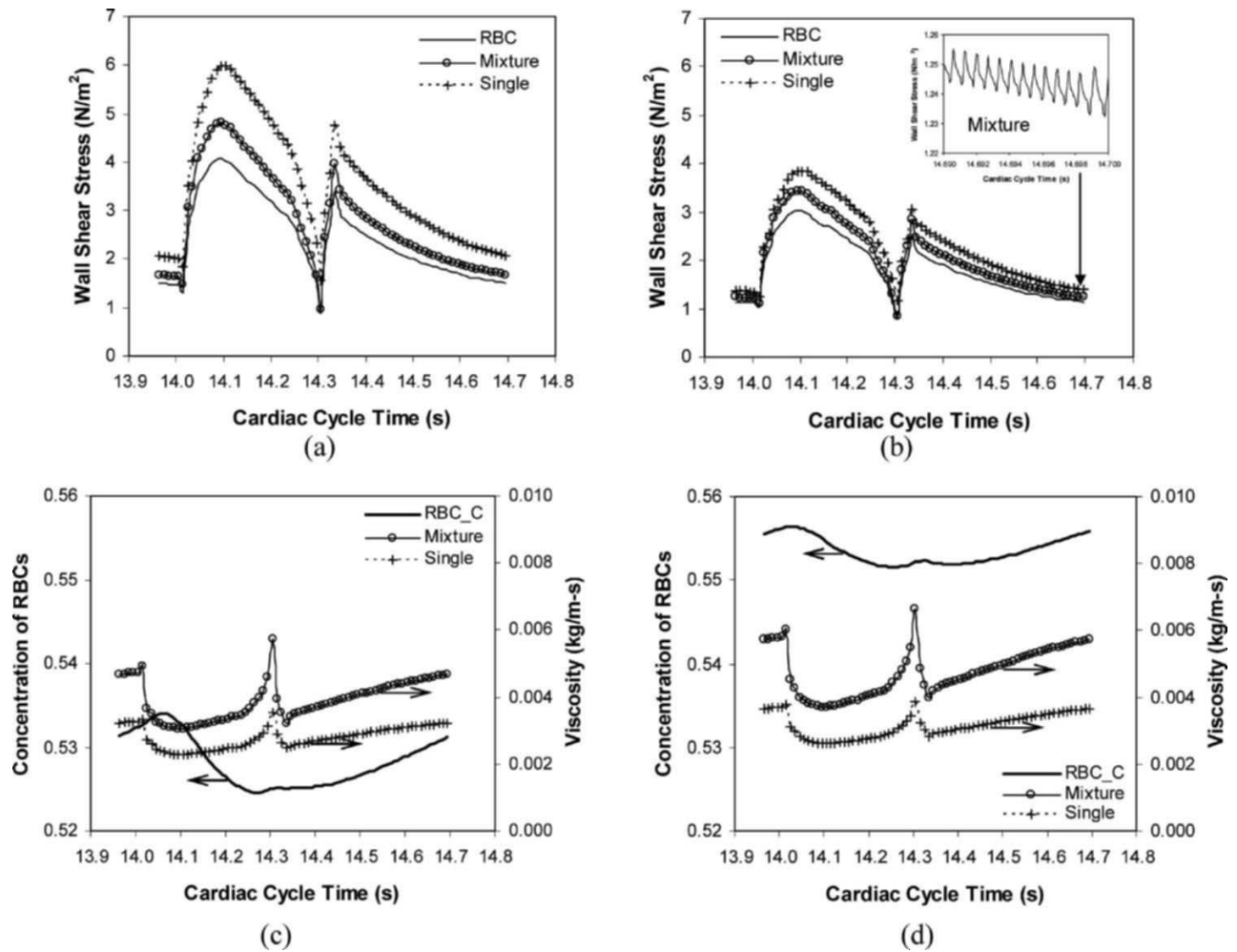
FIGURE 10. Temporal variations of hemodynamic factors near the maximum curvature [point (3)] indicated in Fig. 1. WSS variations at (a) the maximum WSS point [point (3)-2 of Fig. 9] and (b) the maximum RBC buildup point [point (3)-1 of Fig. 9]. Variations of RBC volume fraction and viscosity at (c) the maximum WSS point and (d) the maximum RBC buildup point. The mixture values for the multiphase model are volume-fraction-averaged plasma and RBC values. RBC: WSS due to RBCs computed from the multiphase model. RBC_C: volume fraction of RBCs computed from the multiphase model. Mixture: total WSS or mixture viscosity computed from the multiphase model. Single: WSS or viscosity computed from the single-phase model at the same condition.

the initial RBC volume fraction in the artery (Fig. 12). As the initial plasma viscosity increased, the relative RBC buildup and WSS decreased. Also, as the initial RBC volume fraction increased, the relative RBC buildup decreased, but WSS increased. For nonspherical particles, presented by the shape factor (ϕ) greater than one, both hydrodynamic parameters increased.

DISCUSSION

We have estimated the hemodynamic factors in a realistic human RCA using a multiphase, transient, non-Newtonian, three-dimensional CFD model, FLUENT. The rheological properties of human blood were determined from the non-Newtonian shear-thinning model as a function of shear rate

and hematocrit, based on experimental data (Fig. 2). The model successfully described the concentrated suspension flow of blood in the wider physiological range of hematocrit and the shear rate. For blood flow, the viscosity of normal human RBCs having very high fluidity is different from rigid spheres at the concentrated suspension flow.[21] In normal circulation, the shear rate in the arteries and capillaries is probably above 200 s^{-1}. The deformation of RBCs due to shear rate can be described by Eq. (8), that is, the non-Newtonian shear-thinning model. In a crowded situation at high shear rate, RBCs are more deformable than colliding particulates due to their biconcave shape.[21] The plasma acts as a buffer fluid preventing direct contact between the particulate surfaces. Hence, the interparticle pressure term of Eq. (8) is negligibly small for the suitable range of hematocrit and shear rates in the circulating blood
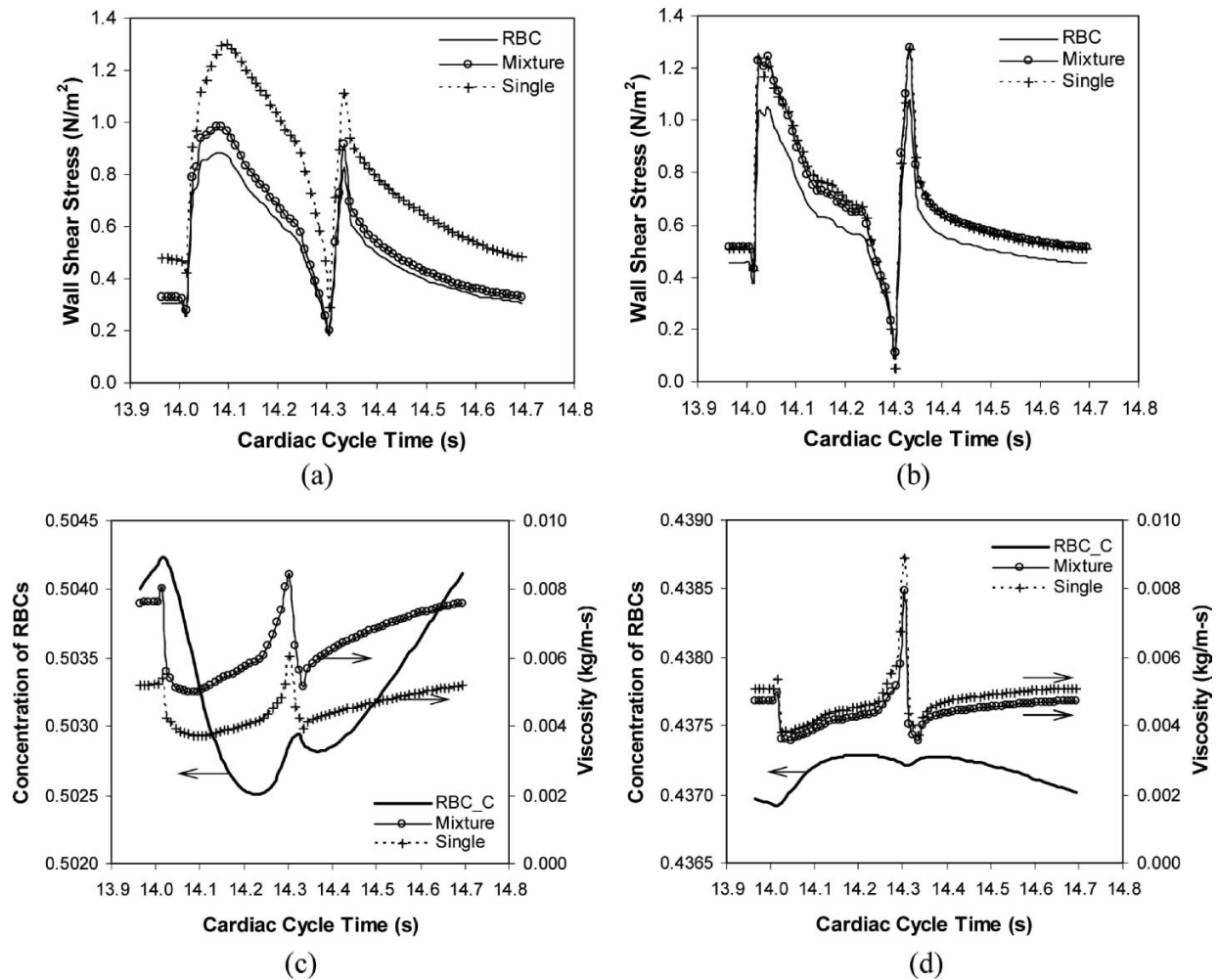
FIGURE 11. Temporal variations of hemodynamic factors near the maximum curvature [point (3)] indicated in Fig. 1. WSS variations at (a) the upflow [point (3)-3 of Fig. 9] and (b) the downflow [point (3)-4 of Fig. 9]. Variations of RBC volume fraction and viscosity at (c) the upflow and (d) the downflow. The mixture values for the multiphase model are volume-fraction-averaged plasma and RBC values. RBC: WSS due to RBCs computed from the multiphase model. RBC_C: volume fraction of RBCs computed from the multiphase model. Mixture: total WSS or mixture viscosity computed from the multiphase model. Single: WSS or viscosity computed from the single-phase model at the same condition.

flow. As a limiting case, the RBC aggregation at low shear rate is assumed to be negligible in this model.

An additional hemodynamic factor of RBC buildup was obtained from the multiphase CFD model: the relationship between WSS and the vessel geometry, where the plaques are known to typically occur. In the single-phase CFD model with a patient-specific geometry for a coronary artery, high WSS was predicted at the stenosis itself on the inside curvature, but when compared with clinical observations,[18,62] low WSS was actually found around the stenosis. Van Langenhove et al.[60] observed helical flow driven by the curvature in such a coronary artery. In an *in vivo* 6-month follow-up study of native arterial segments,[53,54] low WSS was associated with the outward remodeling of atherosclerosis, a feature of vulnerable plaque. In these regions, WSS relatively increased with the increase of plaque

thickness without a change of lumen area. To accurately identify arterial segments bearing vulnerable plaque, more hemodynamic factors in the circulating blood need to be defined.

Hemodynamic factors strongly depend on the non-uniform vessel structure of a patient-specific geometry (Fig. 8). We have conducted a detailed analysis in the curvature region of RCA using the multiphase CFD model. We found that geometry-dependent WSS is associated with RBC buildup of a tortuous reduction area of the maximum arterial curvature, even in the absence of significant lumen obstruction (Figs. 8 and 9). Large- and small-scale oscillations for WSS were observed in the maximum RBC buildup region (Fig. 10). The computation also showed that the oscillatory flow with flow reversal and the secondary flow in this curvature play important roles in local RBC
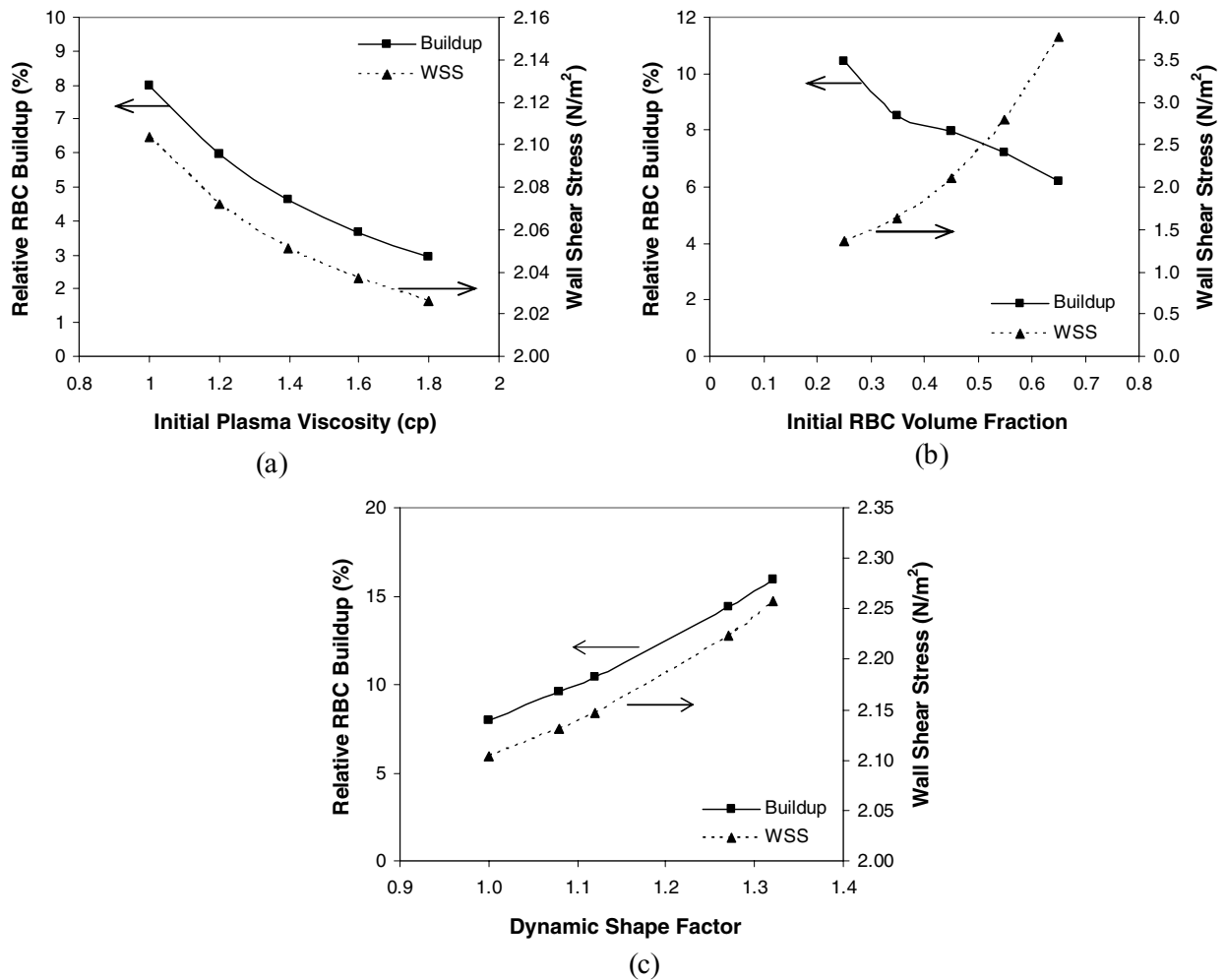
FIGURE 12. Hemodynamic parameters (relative RBC buildup and mixture WSS) computed as a function of (a) initial plasma viscosity, (b) initial RBC volume fraction and (c) shape factor. The values averaged for third cardiac cycle at a point of maximum curvature [point (3)] indicated in Fig. 1.

buildup in a realistic RCA (Fig. 7). Such a flow pattern causes the particulate deposit to shift to the upstream area of the maximum curvature, where low and oscillating WSS was computed (Figs. 10 and 11). As the WSS decreases, the RBC buildup generally increases during the diastole cycle. Hemodynamic conditions having low WSS in specific regions may relate to transport mechanisms of other blood components. In the low WSS region exposed to flow reversal, the endothelium is more easily penetrated by the monocytes and proteins.[12,41,56,58] The prolonged residence time in the recirculation area allows for increased interactions between cellular components and the vessel wall, specifically, at the end of the diastole cycle. Our computational results are consistent with earlier clinical observations for atherosclerotic lesions.[15,53,60] Our findings are consistent with the hypotheses for progression of atherosclerosis described by Stone *et al.*[53]. Our simulations may give further insight into the hemodynamic characteristic for ini-

tial plaque formation and minor obstacle development in the maximum arterial curvature. Clinical observations such as plaque thickness and the degree of stenosis would be necessary.

Hemodynamic features were greatly affected by the rheological nature of blood elements. In normal circulation, the viscosity of whole blood is about 4 cp,[25,37] which is the mixture viscosity computed from the multiphase CFD model. At the high shear rates with an assumption of no cell aggregation, the viscosity of blood is primarily affected by hematocrit and plasma viscosity. The major determinants of plasma viscosity are the concentrations of high-molecular-weight plasma proteins such as fibrinogen and lipoproteins.[20,32,38] The increase of the relative initial plasma viscosity due to the plasma protein concentrations might result in an increase of flow resistance. It affected the RBC fluidity, resulting in a WSS decrease on the inner artery wall for the same hematocrit and mixture viscosity

(Fig. 12). The computed results agree with those of the literature,[20,32,38] where the high value of plasma viscosity indicates susceptibility to coronary disease.

In *in vitro* experiment,[42,43] the presence of RBCs enhanced the leukocyte adhesion to the endothelium monolayer, along with a dramatic increase of leukocyte rolling densities and binding rates. The leukocyte behavior can be influenced by the dispersion due to the RBC-leukocyte collisions in the bulk flow. The cell interactions increased the collision frequency with the endothelium.[43] In the computational simulation, a non-Newtonian shear thinning effect was enhanced by the increase of initial RBC volume fraction (Fig. 12). The shear rate near the wall increased because the velocity distribution has a flatter profile in the center region of the artery. The RBC addition results in a WSS increase on the wall of the artery. The computation predicted that most of the contribution to the WSS is due to the RBCs. Munn *et al.*[43] found that the adding of RBCs may modify the existing paradigm for the pathological response of endothelial cells. We expect the cell interactions, including leukocyte and platelets, in blood flow to play an important role in the early stage of atherosclerotic plaque formation.

In the drag term to account for fluid-particulate interactions, the shape factor is defined as the ratio of the actual resistance force of the nonspherical particle to the resistance force of a sphere having the same volume and velocity. This means that the shape factor for nonspherical particles is generally greater than 1.0, and more drag is experienced by the nonspherical particle in fluid. If it is applicable to biconcave-shaped RBC and/or their agglomerates, WSS might be positively increased, as shown in computational results (Fig. 12). It becomes plausible that the biconcave-shaped RBC has more advantages than the spherical shape in the transport of circulating blood.[21] More studies will be required for nonspherical RBC with flow conditions.

Although this multiphase CFD model does not include the physiologically realistic motions in an artery having several branches, the model has begun to shed light on important hemodynamic phenomena, which have eluded investigators using single-phase CFD models, such as particulate migration and interactions at the surface of endothelial cells. When the model includes monocytes with RBCs, the correlation between low WSS and particulate buildup related to atherogenesis on a realistic artery is expected to be better understood. Additional hemodynamic factors to consider would be the mass transfer between blood and the arterial wall, and the cyclic bending of coronary arteries driven by the heart beat.[48,51]

ACKNOWLEDGMENTS

REFERENCES

[1] American Heart Association. Heart Disease and Stroke Statistics—2004 Update. Dallas: American Heart Association. Available at www.americanheart.org, 2004.

[2] Anderson, T. B., and R. Jackson. A fluid mechanical description of fluidized beds. *I&EC Fundament.* 6:524–539, 1967.

[3] Berger, S., and L. Jou. Flows in stenotic vessels. *Annu. Rev. Fluid Mech.* 32:347–382, 2000.

[4] Berthier, B., R. Bouzerar, and C. Legallais. Blood flow patterns in an anatomically realistic coronary vessel: Influence of three different reconstruction methods. *J. Biomech.* 35:1347–1356, 2002.

[5] Bird, R. B., W. E. Stewart, and E. N. Lightfoot. Transport Phenomena. New York: Wiley, 1960.

[6] Bonert, M., R. L. Leask, J. Butany, C. R. Ethier, J. G. Myers, K. W. Johnston, and M. Ojha. The relationship between wall shear stress distributions and intimal thickening in the human abdominal aorta. *Biomed. Eng. Online* 2:I8, 2003.

[7] Boo, Y. C., J. Hwang, M. Sykes, B. J. Michell, B. E. Kemp, H. Lum, and H. Jo. Shear stress stimulates phosphorylation of eNOS at Ser^{635} by a protein kinase A-dependent mechanism. *Am. J. Physiol. Heart Circ. Physiol.* 283:H1819–H1828, 2002.

[8] Brooks, D. E., J. W. Goodwin, and G. V. F. Seaman. Interactions among erythrocytes under shear. *J. Appl. Physiol.* 28:172–177, 1970.

[9] Caro, C. G., J. M. Fitz-Gerald, and R. C. Schroter. Arterial wall shear and distribution of early atheroma in man. *Nature* 223:1159–1161, 1969.

[10] Cholley, B. P., S. G. Shroff, J. Sandelski, C. Korcarz, B. A. Balasia, S. Jain, D. S. Berger, M. B. Murphy, R. H. Marcus, and R. M. Lang. Differential effects of chronic oral antihypertensive therapies on systemic arterial circulation and ventricular energetics in African-American patients. *Circulation* 91:1052–1062, 1995.

[11] Corson, M. A., N. L. James, S. E. Latta, R. M. Nerem, B. C. Berk, and D. G. Harrison. Phosphorylation of endothelial nitric oxide synthase in response to fluid shear stress. *Circ. Res.* 79:984–991, 1996.

[12] Dai, G., M. R. Kaazempur-Mofrad, S. Natarajan, Y. Zhang, S. Vaughn, B. R. Blackman, R. D. Kamm, G. Garcia-Cardena, and M. A. Gimbrone Jr. Distinct endothelial phenotypes evoked by arterial waveforms derived from atherosclerosis-susceptible and -resistant regions of human vasculature. *Proc. Natl. Acad. Sci.* 101:14871–14876, 2004.

[13] Ding, J., R. W. Lyczkowski, W. T. Sha, S. A. Altobelli, and E. Fukushima. Numerical analysis of liquid-solid suspension velocities and concentrations obtained by NMR imaging. *Powder Technol.* 77:301–312, 1993.

[14] Ding, J., R. W. Lyczkowski, and W. T. Sha. Modeling of concentrated liquid-solids flow in pipes displaying shear-thinning phenomena. *Chem. Eng. Commun.* 138:145–155, 1995.

[15] Ding, Z., H. Zhu, and M. H. Friedman. Coronary artery dynamics in vivo. *Ann. Biomed. Eng.* 30:419–429, 2002.

[16] Dill, D. B., and D. L. Costill. Calculation of percentage changes in volumes of blood, plasma, and red cells in dehydration. *J. Appl. Physiol.* 37:247–248, 1974.

[17] Doriot, P.-A., P.-A. Dorsaz, L. Dorsaz, E. D. Benedetti, P. Chatelain, and P. Delafontaine. In-vivo measurements of wall shear

stress in human coronary arteries. *Coron. Artery Dis.* 11:495–502, 2000.

[18]Feldman, C. L., O. J. Ilegbusi, Z. Hu., R. Nesto, S. Waxman, and P. H. Stone. Determination of in vivo velocity and endothelial shear stress patterns with phasic flow in human coronary arteries: A methodology to predict progression of coronary atherosclerosis. *Am. Heart J.* 143:931–939, 2002.

[19]Fluent Inc. FLUENT User's Guide. Lebanon, NH: Fluent Inc., 2003.

[20]Fuchs, J., I. Weinberger, Z. Rotenberg, A. Erdberg, E. Davidson, H. Joshua, and J. Agmon. Plasma viscosity in ischemic heart disease. *Am. Heart J.* 108:435–439, 1984.

[21]Fung, Y. C. Biomechanics: Mechanical Properties of Living Tissues. New York: Springer, 1993.

[22]Gidaspow, D. Multiphase Flow and Fluidization: Continuum and Kinetic Theory Descriptions. New York: Academic Press, 1994.

[23]Gidaspow, D., J. Jung, and R. K. Singh. Hydrodynamics of fluidization using kinetic theory: An emerging paradigm. *Powder Tech.* 148:123–141, 2004.

[24]Giddens, D. P., C. K. Zarins, and S. Glagov. Role of fluid mechanics in the localization and detection of atherosclerosis. *J. Biomech. Eng.* 115:588–594, 1993.

[25]Gijsen, F. J. H., F. N. Van de Vosse, and J. D. Janssen. The influence of the non-Newtonian properties of blood on the flow in large arteries: Steady flow in a carotid bifurcation model. *J. Biomech.* 32:601–608, 1999.

[26]Glagov, S., E. Weisenberg, C. K. Zarins, R. Stankunavicius, and G. J. Kolettis. Compensatory enlargement of human atherosclerotic coronary arteries. *N. Engl. J. Med.* 316:1371–1375, 1987.

[27]Goldsmith, H. L., and J. C. Marlow. Flow behavior of erythrocytes: II. Particle motions in concentrated suspensions of ghost cells. *J. Coll. Interf. Sci.* 71:383–407, 1979.

[28]Gonzales, S., and T. M. Wick. Hemodynamic modulation of monocytic cell adherence to vascular endothelium. *Ann. Biomed. Eng.* 24:382–393, 1996.

[29]Guenther, C., and M. Syamlal. The effect of numerical diffusion on simulation of isolated bubbles in a gas-solid fluidized bed. *Powder Tech.* 116:142–154, 2001.

[30]Hajjar, D. P., and A. C. Nicholson. Atherosclerosis: An understanding of the cellular and molecular basis of the disease promises new approaches for its treatment in the near future. *Am. Scientist* 83:460–467, 1995.

[31]Hoi, Y., H. Meng, S. H. Woodward, B. R. Bendok, R. A. Hanel, L. R. Guterman, and L. N. Hopkins. Effect of arterial geometry on aneurysm growth: Three-dimensional computational fluid dynamics study. *J. Neurosurg.* 101:676–681, 2004.

[32]Jan, K.-M., S. Chien, and J. T. Bigger. Observations on blood viscosity changes after acute myocardial infarction. *Circulation* 51:1079–1084, 1975.

[33]Jung, J., D. Gidaspow, and I. K. Gamwo. Bubble computation, granular temperatures and Reynolds stresses. *Chem. Eng. Commun.* (in press).

[34]Jung, J., R. W. Lyczkowski, C. B. Panchal, and A. Hassanein. Multiphase hemodynamic simulation with pulsatile flow in a coronary artery. *J. Biomechanics* (in press).

[35]Kleinstreuer, C. Two-Phase Flow: Theory and Application. New York: Taylor & Francis, 2003.

[36]Krams, R., J. J. Wentzel, J. A. F. Oomen, R. Vinke, J. C. H. Schuurbiers, P. J. de Feyter, P. W. Serruys, and C. J. Slager. Evaluation of endothelial shear stress and 3D geometry as factors determining the development of atherosclerosis and remodeling in human coronary arteries in vivo. *Arterioscler. Thromb. Vasc. Biol.* 17:2061–2065, 1997.

[37]Ku, D. Blood flow in arteries. *Annu. Rev. Fluid Mech.* 29:399–434, 1997.

[38]Leonhardt, H., H.-R. Arntz, and U. H. Klemens. Studies of plasma viscosity in primary hyperlipoproteinaemia. *Atherosclerosis* 28:29–40, 1977.

[39]Lightfoot, E. N. Transport Phenomena and Living Systems: Biomedical Aspects of Momentum and Mass Transport. New York: Wiley, 1974.

[40]Longest, P. W., C. Kleinstreuer, and J. R. Buchanan. Efficient computation of micro-particle dynamics including wall effects. *Comp. Fluids* 33:577–602, 2004.

[41]Malek, A. M., S. L. Alper, and S. Izumo. Hemodynamic shear stress and its role in atherosclerosis. *J. Am. Med. Assoc.* 282:2035–2042, 1999.

[42]Melder, R. J., L. L. Munn, S. Yamada, C. Ohkubo, and R. K. Jain. Selectin- and integrin-mediated T-lymphocyte rolling and arrest on TNF-(-activated endothelium: Augmentation by erythrocytes. *Biophys. J.* 69:2131–2138, 1995.

[43]Munn, L. L., R. J. Melder, and R. K. Jain. Role of erythrocytes in leukocyte-endothelial interactions: Mathematical model and experimental validation. *Biophys. J.* 71:466–478, 1996.

[44]Myers, J. G., J. A. Moore, M. Ojha, K. W. Johnston, and C. R. Ethier. Factors influencing blood flow patterns in the human right coronary artery. *Ann. Biomed. Eng.* 29:109–120, 2001.

[45]Nichols, W. W., and M. F. O'Rourke. McDonald's Blood Flow in Arteries. London: Arnold, 1998.

[46]Phillips, R. J., R. C. Amstrong, and R. A. Brown. A constitutive equation for concentrated suspension that accounts for shear-induced particle migration. *Phys. Fluids A* 4:30–40, 1992.

[47]Poppas, A., S. G. Shroff, C. E. Korcarz, J. U. Hibbard, D. S. Berger, M. D. Lindheimer, and R. M. Lang. Serial assessment of the cardiovascular system in normal pregnancy: Role of arterial compliance and pulsatile arterial load. *Circulation* 95:2407–2415, 1997.

[48]Qiu, Y., and J. M. Tarbell. Numerical simulation of pulsatile flow in a compliant curved tube model of a coronary artery. *J. Biomech. Eng.* 122:77–85, 2000.

[49]Sinton, S. W., and A. W. Chow. NMR flow imaging of fluids and solid suspensions in Poiseuille flow. *J. Rheol.* 35:735–772, 1991.

[50]Steinman, D. A. Image-based computational fluid dynamics modeling in realistic arterial geometries. *Ann. Biomed. Eng.* 30:482–497, 2002.

[51]Steinman, D. A., J. S. Milner, C. J. Norley, S. P. Lownie, and D. W. Holdsworth. Image-based computational simulation of flow dynamics in a giant intracranial aneurysm. *Am. J. Neuroradiol.* 24:559–566, 2003.

[52]Steinman, D. A., D. A. Vorp, and C. R. Ethier. Computational modeling of arterial biomechanics: Insights into pathogenesis and treatment of vascular disease. *J. Vasc. Surg.* 37:1118–1128, 2003.

[53]Stone, P. H., A. U. Coskun, Y. Yeghiazarians, S. Kinlay, J. J. Popma, R. E. Kuntz, and C. L. Feldman. Prediction of sites of coronary atherosclerosis progression: In vivo profiling of endothelial shear stress, lumen, and outer vessel wall characteristics to predict vascular behavior. *Curr. Opin. Cardiol.* 18:458–470, 2003.

[54]Stone, P. H., A. U. Coskun, S. Kinlay, M. E. Clark, M. Sonka, A. Wahle, O. J. Ilegbusi, Y. Yeghiazarians, J. J. Popma, J. Orav, R. E. Kuntz, and C. L. Feldman. Effect of endothelial shear stress on the progression of coronary artery disease, vascular remodeling, and in-stent restenosis in humans: In vivo 6-month follow-up study. *Circulation* 108:438–444, 2003.

[55] Sun, C., C. Migliorini, and L. L. Munn. Red blood cells initiate leukocyte rolling in postcapillary expansions: A Lattice Boltzmann analysis. *Biophys. J.* 85:208–222, 2003.

[56] Taylor, C. A., and M. T. Draney. Experimental and computational methods in cardiovascular fluid mechanics. *Annu. Rev. Fluid Mech.* 36:197–231, 2004.

[57] Thubrikar, M. J., and F. Robicsek. Pressure-induced arterial wall stress and atherosclerosis. *Ann. Thorac. Surg.* 59:1594–1603, 1995.

[58] Traub, O., and B. C. Berk. Laminar shear stress: Mechanisms by which endothelial cells transduce an atheroprotective force. *Arterioscler. Thromb. Vasc. Biol.* 18:677–685, 1998.

[59] van de Vosse, F. N., F. J. H. Gijsen, and B. J. B. M. Wolters. Numerical analysis of coronary artery flow. *ASME 2001 Bioeng. Conf.* BED 50:17–18, 2001.

[60] van Langenhove, G., J. J. Wentzel, R. Krams, C. J. Slager, J. N. Hamburger, and P. W. Serruys. Helical velocity patterns in a human coronary artery: A three-dimensional computational fluid dynamic reconstruction showing the relation with local wall thickness. *Circulation* 102:e22–e24, 2000.

[61] Wahle, A., J. J. Lopez, E. C. Pennington, S. L. Meeks, K. C. Braddy, J. M. Fox, T. M. H. Brennan, J. M. Buatti, J. D. Rossen, and M. Sonka. Effect of vessel geometry and catheter position on dose delivery in intracoronary brachytherapy. *IEEE Trans. Biomed. Eng.* 50:1286–1295, 2003.

[62] Wahle, A., M. E. Olszewski, and M. Sonka. Interactive virtual endoscopy in coronary arteries based on multimodality fusion. *IEEE Trans. Med. Imaging* 23:1391–1403, 2004.

[63] Walpola, P. L., A. I. Gotlieb, M. I. Cybulsky, and B. L. Langille. Expression of ICAM-1 and VCAM-1 and monocyte adherence in arteries exposed to altered shear stress. *Arterioscler. Thromb. Vasc. Biol.* 15:2–10, 1995.

[64] Wasserman, S. M., F. Mehraban, L. G. Komuves, R.-B. Yang, J. E. Tomlinson, Y. Zhang, F. Spriggs, and J. N. Topper. Gene expression profile of human endothelial cells exposed to sustained fluid shear stress. *Physiol. Genom.* 12:13–23, 2002.

[65] Wentzel, J. J., E. Janssen, J. Vos, J. C. H. Schuurbiers, R. Krams, P. W. Serruys, P. J. de Feyter, and C. J. Slager. Extension of increased atherosclerotic wall thickness into high shear stress regions is associated with loss of compensatory remodeling. *Circulation* 108:17–23, 2003.

[66] Wojnarowski, J. Numerical study of bileaf heart valves performance. In: International Scientific Practical Conference: Efficiency of Engineering Education in XX Century. Ukraine: Donetsk, May 29–31, 2001.

[67] Zeng, D., Z. Ding, M. H. Friedman, and C. R. Ethier. Effects of cardiac motion on right coronary artery hemodynamics. *Ann. Biomed. Eng.* 31:420–429, 2003.

[68] Zhao, S. Z., B. Ariff, Q. Long, A. D. Hughes, S. A. Thom, A. V. Stanton, and X. Y. Xu. Inter-individual variations in wall shear stress and mechanical stress distributions at the carotid artery bifurcation of healthy humans. *J. Biomech.* 35:1367–1377, 2002.

[69] Zhu, H., and M. H. Friedman. Relation between the dynamic geometry and wall thickness of a human coronary artery. *Arterioscler. Thromb. Vasc. Biol.* 23:2260–2265, 2003.